# Disorder in $La_{1-x}Ba_{1+x}GaO_{4-x/2}$ ionic conductor: resolving Pair Distribution Function through insight from first principles modelling

Mauro Coduri[1,2], Simone Casolo[1], Niina Jalarvo[3,4], Marco Scavini[1,5]

[1] Dipartimento di Chimica, Università degli Studi di Milano, Via C. Golgi 19, I-20133 Milano, Italy

[2] ESRF - The European Synchrotron, 71, Avenue des Martyrs, 38043, Grenoble, France

[3] Neutron Sciences Directorate, Oak Ridge National Laboratory (ORNL), Oak Ridge, TN 37831, USA

[4] JCNS-1, Forschungszentrum Jülich GmbH, 52425 Jülich, Germany

[5] ISTM-CNR and INSTM Unit, Via C. Golgi 19, I-20133 Milano, Italy

**Abstract.** Ionic conduction in dry $LaBaGaO_4$ occurs through the vacant oxygen sites formed by the substitution of Ba for La. The resulting $La_{1-x}Ba_{1+x}GaO_{4-x/2}$ solid solution shows significant disorder characteristics. The local structure was studied using the Pair Distribution Function (PDF) of compositions x=0, 0.20 and 0.30.

Unfortunately, increasing peak overlapping and the number of independent structural parameters make PDF modelling challenging when dealing with low-symmetry phases. To overcome this problem, Density Function Theory was employed to create different structural models, each one with different relative position for the substitutional Ba ion with respect to the oxygen vacancy.

The atomic distributions generated by DFT were used as a starting point to refine experimental PDF data. All models result in the formation of $Ga_2O_7$ dimers, with the Ga-O bridge oriented along $c$ crystallographic axis. At the local scale, the most stable DFT model also provides the best fit of PDF. It accounts for $Ba_{La}$' as $1^{st}$ and $2^{nd}$ neighbor of the vacancy and of the O bridge in the dimer, suggesting that substitutional barium ions act as pinning centers for oxygen vacancies. Above 6 Å the average orthorhombic structure fits the PDF better than the DFT models, thus indicating that $Ga_2O_7$ dimers are not correlated with each other to form extended ordered structures.

The combination of DFT simulations and XRD-PDF refinements was used successfully to model the local atomic structure in $La_{1-x}Ba_{1+x}GaO_{4-x/2}$ thus suggesting that this approach could be positively applied in general to disordered systems.

# 1 Introduction

Ion conductors are of great interest for many renewable energy applications, such as electrolytes for intermediate temperatures fuel cells (Li *et al.*, 2009; Malavasi *et al.*, 2010). Recently, attention is being devoted to solids containing tetrahedral units. Deformations and rotations of the tetrahedra can be a major factor for significant conductivity (Yang *et al.*, 2018; Pramana *et al.*, 2016). This is the case for LaBaGaO$_4$, due to a peculiar "cog wheel" motion involving GaO$_4$ tetrahedral units (Kendrick *et al.*, 2007).

La$_{1-x}$Ba$_{1+x}$GaO$_{4-x/2}$ can exhibit both proton and oxygen ion diffusion through the oxygen vacancies (V$_O$) introduced by substituting Ba for La (Ba$_{La}$') (Kendrick *et al.*, 2010). The ionic conduction occurs via defect migration through intra- and inter-tetrahedral positions (Jalarvo *et al.*, 2013a). The Ba-induced oxygen vacancies are compensated by the relaxation of nearby GaO$_4$ units to form Ga$_2$O$_7$ dimers, with dumbbell shape corner-sharing tetrahedra, maintaining the coordination of Ga ions. The formation of the dumbbells is a key-aspect for the ion migration process, since oxygen vacancies migration requires the breaking and reformation of Ga$_2$O$_7$ dimers to occur (Kendrick *et al.*, 2007, Jalarvo *et al.*, 2013a), while proton transfer occurs through a Grotthus-like mechanism involving intra- and inter-tetrahedron hopping. The presence of Ga$_2$O$_7$ dimers in La$_{1-x}$Ba$_{1+x}$GaO$_{4-x/2}$ structures has been predicted by DFT calculations (Kendrick *et al.*, 2007) and was found to be consistent with the elongated oxygen anisotropic displacement parameters from neutron powder diffraction (Jalarvo *et al.*, 2013a), whilst incoherent neutron scattering was used to elucidate experimentally the diffusion process (Jalarvo et al., 2013b). Previous studies were dedicated mainly to understand the conduction mechanism, with the structural investigation focused on the GaO$_4$ and Ga$_2$O$_7$ units (Hamao *et al.*, 2013, Kendrick *et al.*, 2007, Jalarvo *et al.*, 2013b, Cheng *et al.*, 2017). Differences in the inter-tetrahedra diffusion barriers are possibly influenced by the local cation environment (Kendrick *et al.*, 2007), which, in turn, depends on the structural disorder, the charged Ba$_{La}$' dopant concentration and their mutual interaction. Even though local defect interactions affect the ion migration, no experimental study about the local environment around the doping-induced oxygen vacancies in La$_{1-x}$Ba$_{1+x}$GaO$_{4-x/2}$ has been reported.

The goal of the present work is to fill this gap for x=0, 0.2 and 0.3 by combining atomic Pair Distribution Function (PDF) and density function theory (DFT) calculations to probe the interaction between the dopant species and their effect on the medium-to-long range structure. Although the PDF is a powerful method to probe atomic structures, its modelling is often challenging, as it is strongly sensitive to the choice of the initial structure input for the refining algorithm. In particular, the many possible defect orientations, interactions and mutual arrangements give rise to a large number of possible configurations that may be used as initial guess for the refinement. In this work we have probed several initial defect configurations by generating different models with two oxygen vacancy and dopants placed in different positions. These structural models were first optimized by minimizing their DFT total energy. The obtained different configurations of oxygen vacancies and dopants were tested and used to refine the PDF to determine the optimal structural model. Eventually, as arbitrary constraints are required to reduce the number of structural parameters in low symmetry phases to improve fit reliability, the modelling strategy of PDF data is also discussed.

## 2 Experimental

*Sample preparation.* Samples with compositions $La_{1-x}Ba_{1+x}GaO_{4-x/2}$ with x = 0, 0.20, 0.30, were prepared from high purity $La_2O_3$, $BaCO_3$ and $Ga_2O_3$. The powders were mixed in due stoichiometry and heated to 1400 °C in air for a day. Dehydration was obtained by heat-treating at 1100 °C for 4 h with flowing dry $O_2$. Afterwards, the samples were cooled to room temperature at the rate of 5 °C/min.

*PDF data collection.* X-Ray Powder Diffraction (XRPD) data for PDF analysis were collected at the ID15 beamline of the ESRF at *T*= 120 K on samples with composition $La_{1-x}Ba_{1+x}GaO_{4-x/2}$ with x = 0, 0.20 and 0.30. Low temperature was chosen to minimize thermal motion. Incident X-ray wavelength was $\lambda$=0.1420 Å (*E*~87 keV). A mar345 image plate detector was placed perpendicular to the incident beam at ~15 cm distance from the sample. A NIST $CeO_2$ reference standard was used for detector calibration using fit2d (Hammersley *et al.*, 1996).

The powders were packed in kapton capillaries with 2 mm diameter inside a glove bag filled with dry nitrogen. The capillaries were inserted into a brass pinhole and mounted on a goniometer head, which was rotating during acquisition to increase powder randomization. 0.6 seconds per frame was chosen as optimal exposure time, since longer exposures would lead to detector saturation. 24 frames were merged together to increase the signal-to-noise ratio, especially in the high-*Q* region. Considering the readout time required for the camera to process the data, acquisition for each sample took on average half an hour.

Here we describe the PDF using the G(*r*) formalism, which indicates the probability of finding a pair of atoms separated by a distance *r* with an integrated intensity dependent on the pair multiplicity and the scattering factors of the elements involved (Egami & Billinge, 2003). G(*r*) is experimentally determined via sine Fourier transform of the total scattering function *S*(*Q*) according to:

$$G(r) = \frac{2}{\pi} \int_0^\infty Q[S(Q) - 1] \sin(Qr)\, dQ \qquad (1)$$

S(*Q*) corresponds to the coherent scattering coming from the sample (Bragg peaks + diffuse scattering) after proper normalization. The background signal, given by the empty kapton capillary, is scaled and subtracted, while other corrections (absorption, incoherent scattering, polarization, etc..) are performed via software. Generally, F(*Q*) $(F(Q) = Q[S(Q) - 1])$ is plotted instead of S(Q) to check data quality since the former highlights oscillations and noise, if present, at high *Q*. G(*r*) curves were computed with the software pdfgetX2 (Qui *et al.*, 2004a). *F*(*Q*) were truncated to $Q_{max}$=25 Å$^{-1}$ as at larger *Q* values the effect of noise becomes significant. Refinements were performed using PDFgui (Farrow *et al.*, 2007) which assesses the degree of accuracy of the refinement by the agreement parameter Rw:

$$R_w = \sqrt{\frac{\sum_{i=1}^n w(r_i)[G_{obs}(r_i) - G_{calc}(r_i)]^2}{\sum_{i=1}^n w(r_i)G_{obs}^2}} \qquad (2)$$

As a short sample to detector distance was chosen, large $Q_{max}$ can be reached at the expense of the resolution of the XRPD pattern, with consequent damping and broadening of PDF peaks with the interatomic distance *r*. (Qiu *et al.*,

2004b) The corresponding parameters in PDFgui (qdamp and qbroad) were determined to be 0.061 and 0.045, respectively, using a $CeO_2$ NIST standard. PDF peaks are observed up to 3-4 nm. Consequently, reliable PDF analysis is limited to interatomic distances within ~2 nm.

*Calculations.* Periodic Density Functional Theory (DFT) calculations were performed with the VASP program (Kresse & Hafner, 1993; Kresse & Furthmüller, 1996), with periodic boundary conditions. A gradient corrected spin polarized PBE functional (Blöchl, 1994) was used with a basis set of plane waves limited to an energy cutoff of 600 eV. Core contributions to the electronic structure were included via projector augmented wave (PAW) potential method (Perdew *et al.*, 1996). Ionic relaxations were performed allowing full freedom of the length and orientation of lattice vectors and were considered to be converged when the forces acting on each ion were all below 0.01 eV/Å. As starting point for our DFT geometry optimization we used a cell consisting of the experimental structure of $LaBaGaO_4$ at full occupancy, made of 4 formula units. No significant changes were found when optimizing an 8-unit-cell model. The DFT structural model is consistent with the structure reported in the literature, as described below.

As to Ba-rich samples, we tested four different defect models, each involving different relative positions for $Ba_{La}$' and $V_O$. A $1\times1\times2$ supercell was considered in order to fulfill the stoichiometry corresponding to $La_{1-x}Ba_{1+x}GaO_{4-x/2}$ x=0.25, consisting of 8 formula units and a $V_O$ was set at one of the four possible O3 sites (green balls in Figure 1), which we found to be the most favorable in agreement with previous studies (Kendrick *et al.*, 2007). One $Ba_{La}$' was placed randomly in the cell, then the second was set to the farthest La site, as $Ba_{La}$' may repel each other: We then have two $Ba_{La}$' *per* unit cell in DFT calculations, with $La_6Ba_{10}Ga_8O_{31}$ composition. The reciprocal space for this model was sampled in the calculations by a Γ-centered k-point mesh in which the maximum distance between points is $0.25\times2\pi|a|$, for each lattice vector direction. This corresponds to a 3x4x3 Γ-centered grid for the supercell of $La_{1-x}Ba_{1+x}GaO_{4-x/2}$ at x=0.25.
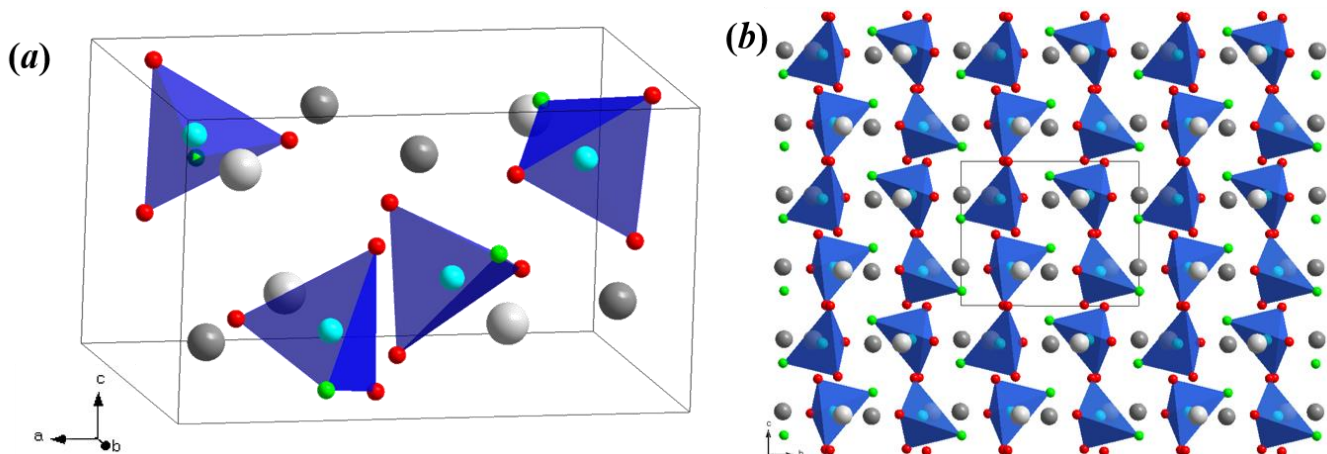


**Figure 1**. (*a*) Sketch of $LaBaGaO_4$ unit cell. O ions are in red, Ga ions in cyan, Ba and La ions in light and dark grey, respectively. $GaO_4$ tetrahedra are displayed in blue and green balls highlight the O3 site. (*b*) View of tetrahedral connectivity along *a*. The unit cell is displayed as black solid line.

4

# 3 Results and Discussions

Stoichiometric LaBaGaO$_4$ at room temperature is orthorhombic with space group P2$_1$2$_1$2$_1$ and lattice parameters *a* ~10.014 Å, *b* ~ 7.265 Å and *c* ~ 5.910 Å (Kendrick *et al.*, 2007). The unit cell, composed of GaO$_4$ distorted tetrahedral units not directly connected with each other, is sketched in Fig. 1(*a*), while an overview of the tetrahedral connectivity is shown in the panel (*b*). A view from different directions is reported in the supporting material, together with a sketch of the unit cell with Ba and La polyhedra. According to Rüter *et al.* (Rüter *et al.*, 1990) a single 4a site is characteristic for each of La (0.051, 0.496, 0.124), Ba (0.670, 0.334, 0.240) and Ga (0.334, 0.282, 0.264); whereas O ions lie on four different 4a sites. Hereafter this will be deemed as the *reference* structure.

The *average* structure will be considered as the *reference* structure with Ba/La and O occupancy factors set according to stoichiometry. In the following section we describe the experimental PDF raw data, which are first refined using the *average* structural models, then employing the DFT structures.

## 3.1 PDF - raw data

The *F*(Q) curves are reported in Fig. 2 (*a*) together with the corresponding PDF (*b*). The *reference* structure of LaBaGaO$_4$ was used to compute the partial PDFs (Fig. 2c), *i.e.* the PDFs resolved for each atom pair. The background slope was subtracted for facilitating comparisons among different atom pairs. Contributions from O-O pairs were not shown, since they are clearly negligible. Ga-Ga correlations are not reported here as they occur only on a larger *r* range ($r_{Ga-Ga}$ > 4.5 Å). It is evident that only the first Ga-O pair, centered at 1.84 Å and well apparent in all the samples, does not overlap with other peaks. Indeed La-O and Ba-O pairs occur at ~2.5 and ~2.9 Å, respectively, while all metal-metal distances are larger than 3.2 Å.

In general, X-ray PDFs are most sensitive to metal-metal correlations, especially those between La and Ba ions, which occur at around 4 Å. At larger interatomic distances the PDF signal originates mostly from metal-metal contacts.
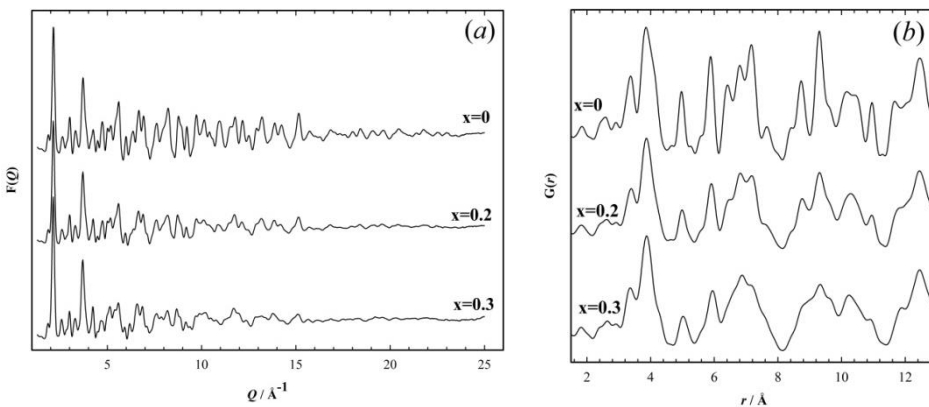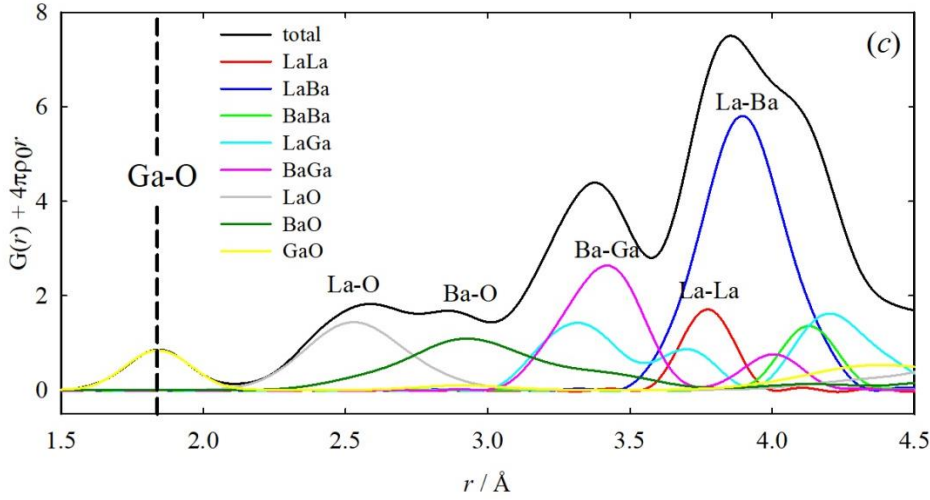
**Figure 2.** (*a*) F(*Q*) and (*b*) G(*r*) curves of samples collected at 120K. (*c*) Partial calculated G(*r*) curves for *reference* x = 0.

Fig. 2 (*b*) shows that all samples share a very similar local environment (*r*<4 Å). The signal of the first peak (1.84 Å) is invariant with doping, thus suggesting the preservation of rigid $GaO_4$ units, as already observed through absorption spectroscopy (Giannici *et al*., 2009; Giannici *et al*., 2011). Also, Fig. 2(*b*) shows well resolved Ba-O and La-O distances which are maintained upon Ba/La substitution. PDF peaks become much broader especially for *r* > 5 Å and for the sample with the highest Ba doping level (x=0.30). Since experimental PDF were collected at the same temperature, the increasing peak broadening indicates a larger distribution of interatomic distances, *i.e.* static disorder.

**3.2 PDF - *average* model**

The *reference* orthorhombic model of $LaBaGaO_4$ was tested against the experimental PDF curves for pristine (x=0) and doped samples. The original atomic positions of $LaBaGaO_4$ reported in (Rueter *et al*., 1990) were kept fixed as the refinement of atomic coordinates led to non-negligible correlations among parameters and did not improve significantly the fit. The refinements are shown in Fig. 3. Lattice parameters, isotropic mean square displacements parameters (*msd*) and residual Rw are listed in Table 1. La and Ba occupancies were modified to account for the actual stoichiometry.

**Table 1.** Results of real space refinements in the 1.5 to 10 Å range using a *reference* orthorhombic model modified according to stoichiometric composition.

| x | lattice parameters / Å | | | *msd* / Å$^2$ | | | | Rw |
|---|---|---|---|---|---|---|---|---|
| | *a* | *b* | *c* | Ba | La | Ga | O | |
| 0 | 10.006(3) | 7.254(1) | 5.898(2) | 0.0063(1) | 0.0041(1) | 0.0081(1) | 0.035(1) | 0.085 |
| 0.20 | 10.071(3) | 7.310(3) | 5.876(2) | 0.0162(2) | 0.0081(2) | 0.0266(3) | 0.060(4) | 0.156 |
| 0.30 | 10.063(8) | 7.414(6) | 5.841(6) | 0.0278(2) | 0.0184(2) | 0.0454(4) | 0.040(6) | 0.201 |

The PDF of pristine $LaBaGaO_4$ is fully consistent with the literature model and our DFT data, while the fit quality worsens with increasing Ba-substitution. A clear lattice expansion upon Ba insertion is observed along the *b* axis in keeping with other works (Kendrick et al., 2007; Giannici *et al*., 2011; Hamao *et al.*, 2013). The main effect of Ba substitution is the increase of *msd*, according to the broadening of PDF peaks, which suggests the presence of static disorder (Scavini *et al*., 2012; Coduri *et al*., 2018a). This agrees with the outcome of absorption spectroscopy investigations, which indicated significant disorder in respect to the metal-metal distances (Giannici *et al*., 2011). However, as these distances lie at around 4 Å, EXAFS is not suitable for their accurate determination. These results indicate that the substitution of Ba for La modifies the interatomic-distances distribution compared to the pristine sample. Therefore, a different model, accounting for the local relaxation around defects, is called for.

### 3.3 DFT models for doped $LaBaGaO_4$

Four different structures of $La_{1-x}Ba_{1+x}GaO_{4-x/2}$ at x=0.25 were generated and optimized by DFT calculations and all of them show a preferential formation of $V_O$ to the O3 site (4a, x~0.29, y~0.50, z~0.40) in $P2_12_12_1$ space group, in agreement with recent theoretical and experimental findings (Kendrick *et al.*, 2007, Jalarvo *et al.*, 2013a). This leads to the formation of $Ga_2O_7$ moieties, one per Vo, oriented with their major axis along |*c*| and induces a slight distortion of the lattice vectors to a monoclinic cell. These distortions are though very subtle (<1°) and were disregarded as they could be ascribed to numerical inaccuracies of DFT. For this reason, we will not discuss DFT lattice parameters but only ionic positions. An overview of the four optimized DFT models is given in Fig. 4. The main difference between each of the four DFT-generated structural models lies in the relative positions of substitutional Ba-ions (yellow spheres) with respect to the oxygen vacancy (black sphere). Substitutional Ba ions were considered as 1st and 2nd, 2nd and 2nd, 1st and 3rd and 2nd and 3rd cation neighbors of the vacancy. The relative positions of defects are listed in Fig. 4 along with the corresponding energy, expressed as difference with respect to the most stable model (model 2), whose energy was set to zero.

Each model was tested twice, varying the absolute position of the atoms before the minimization process. This tested the reproducibility of the calculation and the following fit procedure.
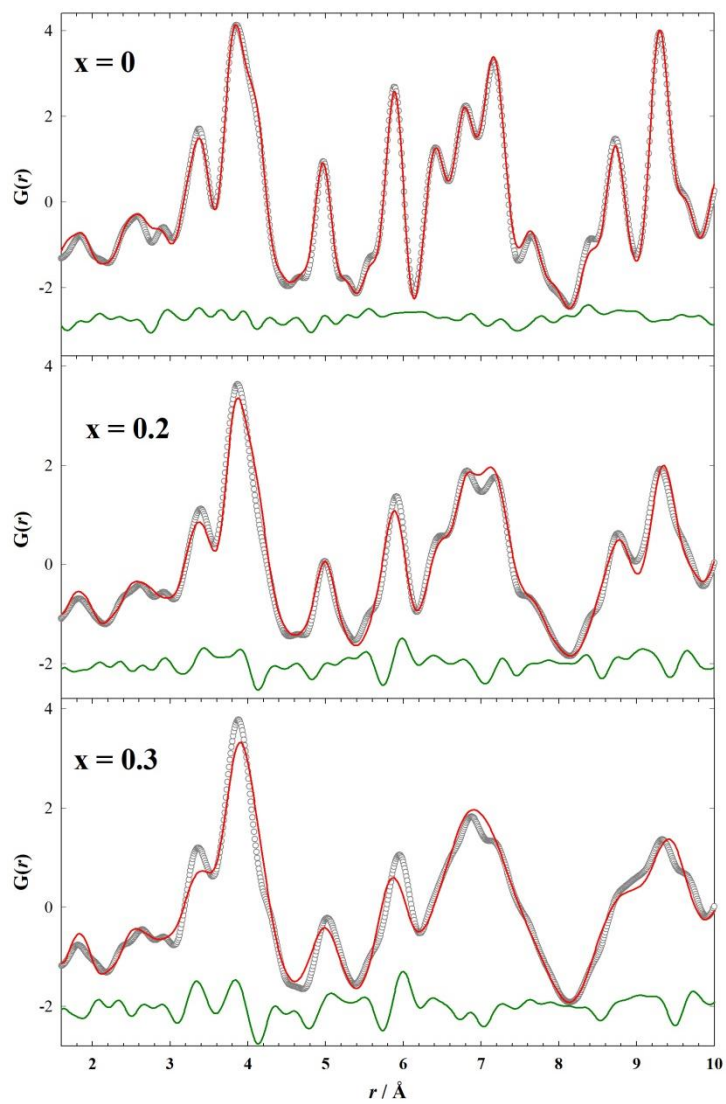
**Figure 3.** Real space refinements of *average* long range model against local scale PDF curves.
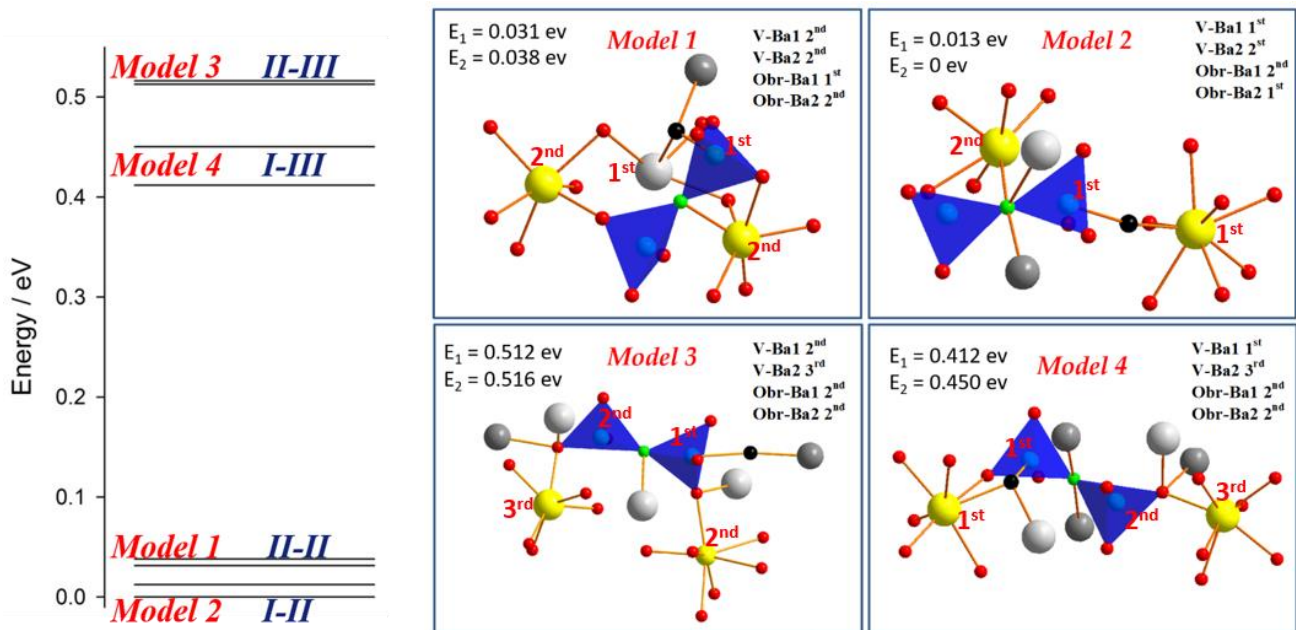
**Figure 4**. Examples of the different configurations as found after the relaxations of the models and plot on energy scale. O ions are in red, Ga ions in cyan, Ba and La ions in light and dark grey, respectively. The oxygen vacancy (black) is located with reference to the position of the corresponding O site in the pristine sample. The O ions which act as a bridge between Ga ions are in green, whilst substitutional Ba ions are in yellow. The relative position of substitutional ions (Ba1 and Ba2), oxygen vacancy (V) and oxygen bridge (Obr) are also indicated, together with the relative energy of the models. Red ordinal numbers refer to the distance of the cations with respect to the oxygen vacancy. The lines connecting atoms are a guide to the eye rather than an indication of a bond.

According to the energies derived from DFT, Model 2 is the most reliable. It exhibits a compact aggregation of the defects arising from $Ba_{La}$' substitution: the bridging O (Obr) is separated by the oxygen vacancy just by one Ga ion; the two substitutional $Ba_{La}$' appear as $1^{st}$ and $2^{nd}$ neighbors of both the oxygen vacancy and the Obr.

Model 1 has similar energy as model 2, indeed they differ for $Ba_{La}$' being $2^{nd}$ cation neighbor of the vacancy rather than $1^{st}$ neighbor. The other two models exhibit only one substitutional Ba as a $1^{st}$ or $2^{nd}$ cation neighbor of $V_O$ and were found less stable from DFT calculations. The four DFT structural models were used as starting guess for the analysis and interpretation of PDF data. A list of distances of interest, with respect to the position of the O bridge in the $Ga_2O_7$ unit and the oxygen vacancy, is reported in the supporting material, Table SI1. $Ga_A$ and $Ga_B$ stand for the two Ga ions involved in the $Ga_2O_7$ unit.

9

The DFT data show that the $Ga_2O_7$-dimer formation promotes the elongation of Ga-O bond lengths along *c* axis, with a corresponding contraction of some Ga-O not involving Obr. Yet, this is not recognizable from direct inspection of the experimental PDF curves, since only two Ga-O distances over 32 in the 2x1x1 supercell are involved. It turns out that such an elongation is not apparent in the experimental curve.

The Ga-O bond angles are reported in supporting material, Table SI2. The formation of the $Ga_2O_7$-units does not affect significantly the bond angles within the tetrahedra, where a wide distribution, from 98 to 130 deg. is already observed in the undoped sample. Noticeably, for each DFT model, the smaller and the bigger angles concern the bridging oxygen.


### 3.4 Matching calculations and experimental PDFs

As the fit of the *average* model against experimental PDFs of Ba-rich samples is not satisfactory, the DFT models were employed as starting point. Even so, a major problem exists when matching calculations and experimental PDFs, as in DFT models all atomic positions are independent of each other. The simultaneous refinement of the atomic coordinates of all 55 atoms in the supercell would clearly lead to major correlations among refined parameters. It turns out that some constraints are necessary.

The most suitable refinement strategy has to be selected according to the complexity of the unit cell and to the accuracy required. Different approaches are reported in the literature. When the available models involve noteworthy variation of energy, DFT can be used to discern the most stable atomic arrangement to confirm, or exclude, the PDF results. Page *et al.* (Page *et al.*, 2007) observed by PDF short range cis-$TaO_4N_2$ polyhedra in $BaTaO_2N$ and found that this configuration had the lowest energy among the models considered. Concerning gallate conductors, a similar approach was used in (Kitamura et al, 2013) to define the configuration of oxygen vacancies in $LaSrGa_{1-x}Mg_xO_{4-\delta}$, which is composed of a framework of $GaO_6$ octahedra.

The above strategy, however, uses DFT as a further technique to confirm PDF results and not for direct PDF modeling. An iterative DFT and PDF minimization procedure was used by White *et al*. (White et al., 2010). The relaxed positions from DFT were used as a starting model to fit experimental PDFs, using the output once again for DFT minimization, and so on recursively. This approach is helpful especially when the starting model is far away from the correct solution.
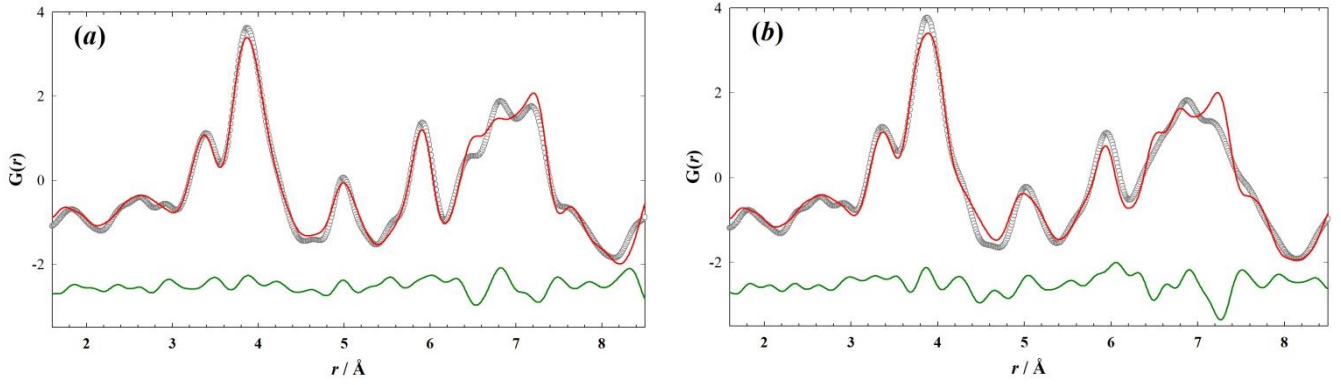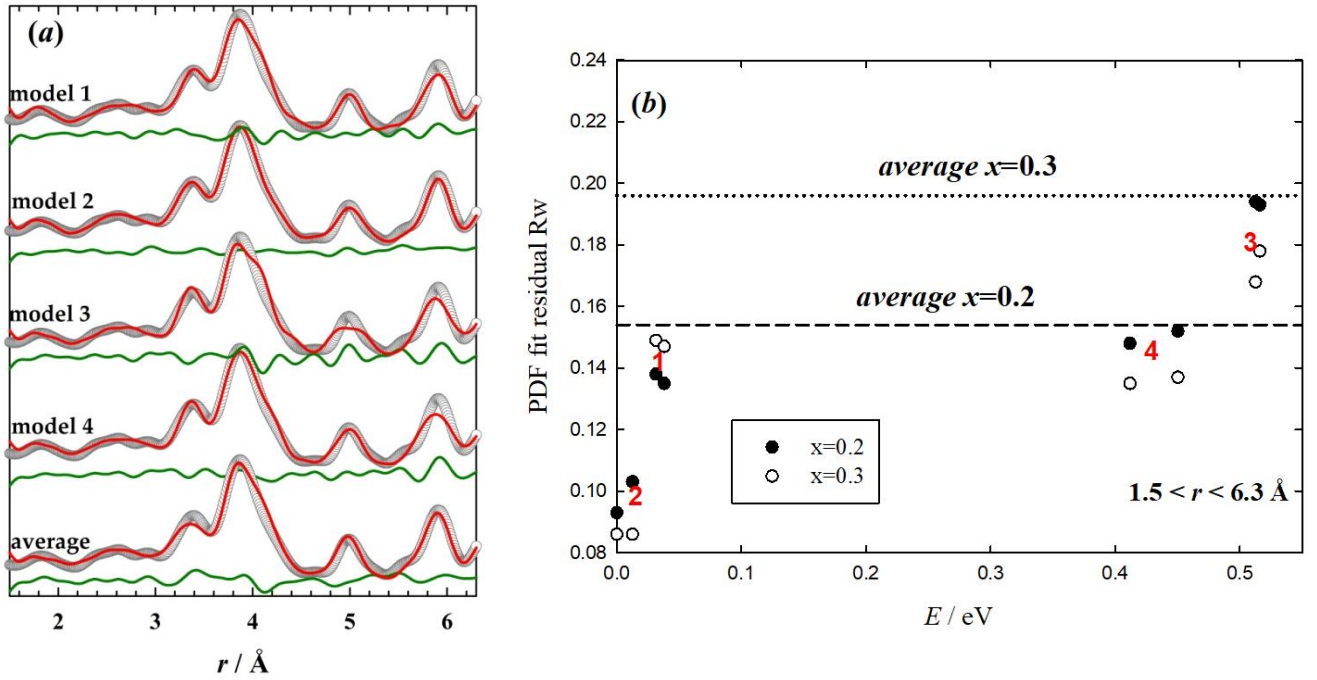
**Figure 5.** Best fits using model 2 against the experimental PDFs of samples (*a*) x=0.2 and (*b*) x=0.3. Empty circles: experimental data; red solid line: calculated PDF; green line: residual.

When the *average* structure is known, or whenever it can be easily foreseen theoretically, DFT can be used to predict the relaxation following a chemical modification such as the introduction of an external atom or a vacancy. In ref (Mancini *et al.*, 2012), the effect of extra oxygen in the structure of melilite was investigated by first relaxing the structure by DFT, then using the returned model to fit PDF data by keeping all atomic positions fixed but the ones closed to the interstitial atom. *msd* were refined and used as a reference to check the reliability of the fit.

For the present investigation we used a similar, yet different, strategy. All atomic coordinates were kept fixed to those obtained from the four DFT models. *msd* were set to the values corresponding to the pristine sample (see Table 1) and not refined. Therefore, only the vibrational contribution to *msd* is considered and the disorder observed as large *msd* using the *average* model is accounted in terms of dispersion of atomic positions, which were fixed to the values computed by DFT. This was done on purpose to minimize correlations, as PDF peaks of samples x=0.2 and 0.3 are very broad. Only lattice parameters, scale factor and a parameter accounting for the correlated motion of nearest neighbors were refined. Lattice parameters have to be necessarily refined because of the low accuracy in their determination through DFT and for the uncertainty of the wavelength of the PDF experiment arising from the correlation with the sample-to-detector distance.

Fig. 5 displays the fit of the best DFT model (model 2) for x=0.2 (*a*) and x=0.3 (*b*) in the 1.5<*r*<8.5 Å interatomic distance range. For both samples, model 2 fits well the local scale (*r* < ~6 Å), while the fit is poor for larger interatomic distances. This could be somewhat expected, as the model used in DFT calculations (which uses periodic boundary conditions) has its smallest lattice parameters of |a|~ 7.4 Å, meaning that each lattice position in this theoretical model is about |a|=7.4 Å far apart from its periodic replica. An opposite behavior is observed for the *average* model (see Fig. 3), which fits much better the PDF curves at larger interatomic distances.

**Figure 6.** (*a*) Refinements of the relaxed models and of the *average* structure against experimental PDF curves of specimen x=0.2 (*a*) in the 1.5 < *r* < 6.3 Å. Empty circles: experimental data; red solid line: calculated PDF; green line: residual. (b) Residual of the fit of the calculated DFT models against experimental PDF curves for x=0.2 (full circles) and x=0.3 (empty circles), compared to the *average* model (dashed and dotted lines for x=0.2 and x=0.3, respectively) within 1.5 < *r* < 6.3 Å.

For these reasons, in the following we discuss separately the very local scale (*r* < 6.3 Å) and a larger interatomic distance range (6.3 Å < *r* < 13 Å). Further interatomic distances are not considered, since instrumental effects (peak damping and broadening) become increasingly important.

The fits for the four models against the experimental PDF on the local scale of sample x=0.2 are shown in figure 6 (*a*). The corresponding fit residuals $R_W$ are given in Fig. 6 (*b*) for the samples x=0.2 (full circles) and x=0.3 (empty circles) as a function of the minimum energy obtained through the calculations.

For both samples, the most stable DFT model guarantees also the best fit, whereas models 3 and 4, which exhibit higher energy by ~0.4-0.5 eV, give a poorer fit (higher residual), especially model 3 where the $Ba_{La}$' lie as far as possible from the $V_O$.

It turned out that two models with very similar energy (models 1 and 2) can be easily distinguished applying PDF analysis to experimental data. Even a simple qualitative inspection of Fig. 6 (*a*) reveals that model 2 provides the best fit. The two models having such similar energy suggest that the short-range interactions do not change significantly. On the other hand, the PDF from X-ray is mostly sensitive to the contributions of cations. From the fits reported in Fig. 6 (*a*) the main differences between models 1 and 2 are related to the high-*r* tail of the main peak, at ~4.3 Å, and to the peak at ~5.9 Å.

In order to associate these regions to the corresponding atom pairs, Figure 7 (*a*) reports the partial PDFs for the different atom pairs of interest in this region calculated for model 1 and 2 as black and red solid lines, respectively. The main PDF signal is given by La-Ba pairs, which are, tough, very similar for all the models considered. The

dashed vertical line in Fig. 7 (*a*) is a guide to the eye referring to the *r* positions where model 1 fails, compared to model 2, to fit correctly experimental data. They correspond to maximum values in the residual curve of model 1, in Fig. 6 (*a*). The difference at 4.3 Å is ascribed to a different distribution of La-Ga pairs, while the peak at ~5.9 Å, underestimated by model 1, concerns only Ba-Ba pairs.
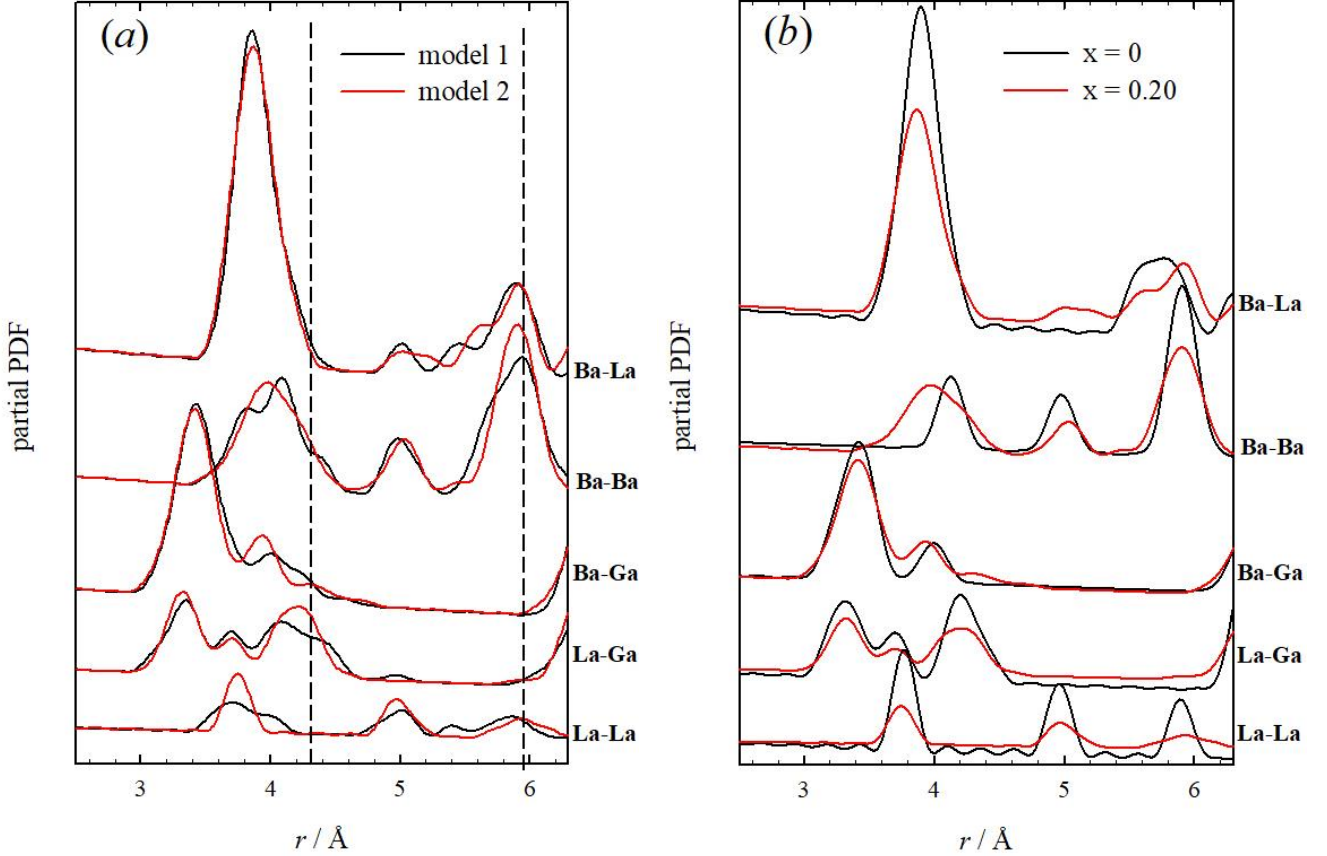


**Figure 7.** (*a*) Partial PDFs calculated from the output of PDF refinements based upon DFT model 1 (black) and 2 (red) for sample x=0.2. Vertical dashed lines indicated major differences between calculated models. (*b*) Partial PDFs extracted for x=0 (black) and DFT model 2 applied to sample x=0.2 (red).

This highlights the importance of combining experimental and theoretical methods to investigate defects in materials as two structural models with relatively similar stabilities (only 44 meV of difference between the energies of model 1 and 2) give significantly different (~50% of Rw) fits to the experimental PDF data (residues of ~0.1 vs 0.15). Indeed, when only the *average* model is available as a starting point, an intensive use of parameters constrains is required, as the number of independent parameters to refine is limited by the width of the *r* range considered (Farrow *et al.*, 2011). This poses serious limitations to the modeling of complex systems where disorder is limited to a small spatial region. In addition, calculations give a complete picture of the local structure, while PDF from X-ray data is mostly sensitive to the displacements of heavy ions. As the models have different energies, defect interactions are not negligible. As reported in (Kendrick et al., 2007), ignoring defect interactions affects the estimation of the activation energy for ionic migration. Among the different models, the stability of the defect configurations increases by placing both substitutional $Ba_{La}$' and Obr next to the oxygen vacancy. The ability of X-rays to probe heavy elements

corresponds also to its main limitation, as experimental PDF curves are less sensitive to O ions than heavier cations, while a more direct structural evidence about O ions can be gained through neutron diffraction. In fact, as observed in Fig. 6(*a*), even model 2 does not fit perfectly the peaks at low *r*-values, which have low intensity. On the other hand, it should be reminded that atomic positions and *msd* were not refined, therefore the PDF fit residuals provides an indication about the goodness of the DFT model. We expect that using neutron diffraction the residual will be more sensitive to O positions and less sensitive to cations, providing a complementary information to X-rays.
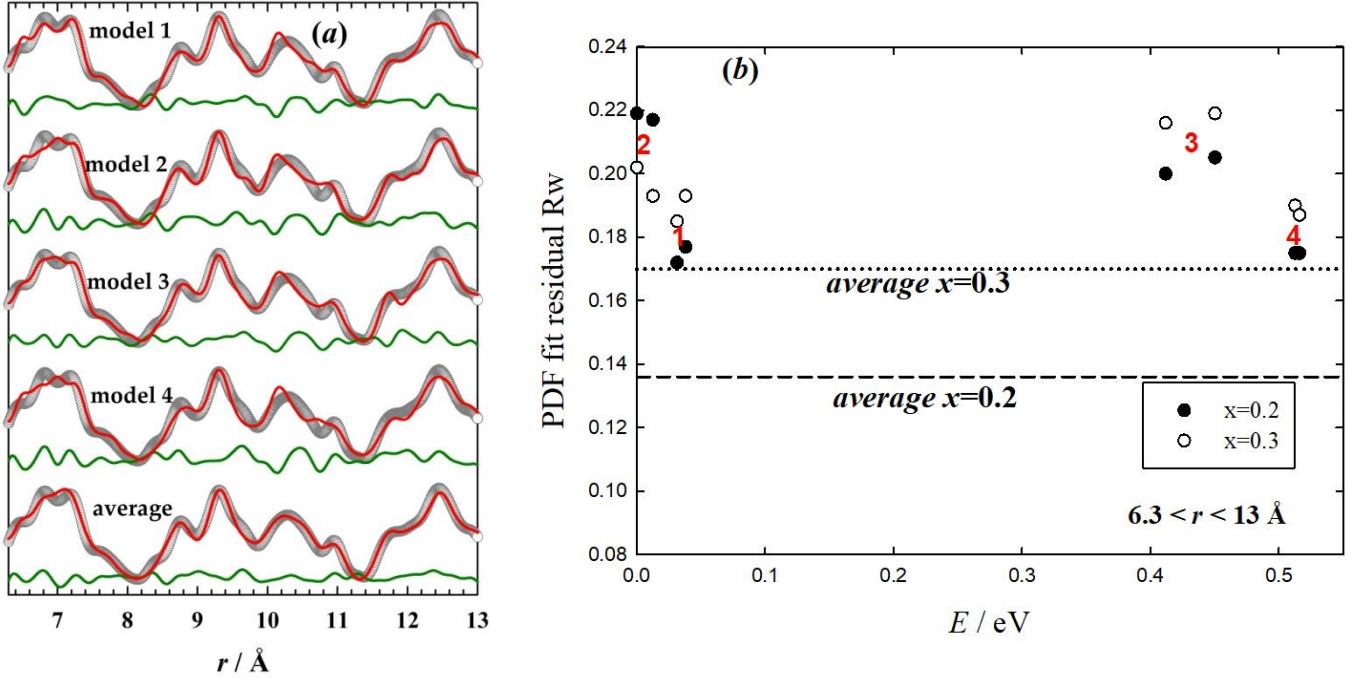


**Figure 8.** (*a*) Refinements of the relaxed models and of the *average* structure against experimental PDF curves of specimen x=0.2 (*a*) in the 6.3 < *r* < 13 Å. Empty circles: experimental data; red solid line: calculated PDF; green line: residual. (b) Residual of the fit of the calculated DFT models against experimental PDF curves for x=0.2 (full circles) and x=0.3 (empty circles), compared to the *average* model (dashed and dotted lines for x=0.2 and x=0.3, respectively) within 6.3 < *r* < 13 Å.

The same approach can be exploited to highlight and understand the difference in the interatomic distances induced by Ba-addition. The partial PDFs extracted from the best fit of sample x=0 and x=0.2 are displayed in Fig. 7 (*b*). Sample x=0.3 is not reported since the interatomic distribution is very similar as sample x=0.2, given that the atomic positions are calculated from the same model.

Whereas the 1$^{st}$ neighbor Ba-Ba pairs shrink significantly upon Ba-insertion, the distances of the pairs involving Ga, especially Ba-Ga, are much less affected. Also, La-La correlations occur at the same interatomic distances even though their distribution upon Ba-doping becomes much larger. It turns out that La-substructure becomes more disordered consequently to Ba substitution. As the migration process in $La_{1-x}Ba_{1+x}GaO_{4-x/2}$ conductors involves the breaking and reorganization of $Ga_2O_7$ dimers (Kendrick *et al.*, 2007, Jalarvo *et al.*, 2013a), it is affected significantly by the local structure. Indeed, a disordered structure with short metal-metal distances, *i.e.* smaller cavities, increases the activation energy for the ion migration (Cheng *et al.*, 2017).

The PDF provides information also on a wider length scale, inaccessible by DFT alone. The refinements performed in the $6.3 < r < 13$ Å range and the corresponding fit residuals are shown in Fig. 8 (*a*) and (*b*), respectively. For both samples the *average* model performs better than the relaxed ones. Compared to the local scale, the fit of the *average* model enhances, while DFT models perform poorly.

The DFT model describes well just the first coordination shells, where no obvious longer-range ordering occurs. It turns out that the observed disorder consists of small 'rigid' units on few Å scale containing dumbbells $Ga_2O_7$. These units are not correlated with each other; therefore they do not order long range. Should the $Ga_2O_7$ dumbbells order long range lengthening the list of non equivalent sites, the phase symmetry would be reduced. The consequent change of the axes vectors (*e.g.* the doubling of the *c* axis used to build the supercells used for DFT modelling) would produce additional signals in the diffraction patterns, which were not observed here, nor have they ever been reported.

The uncorrelated distribution of domains ordered only at the nanoscale is typical for disordered systems (Chung *et al.*, 2005; Dagotto, 2005). Whether trapping oxygen vacancies locally in ionic conductors (Coduri et al., 2013; Coduri *et al.*, 2018b) or limiting polarization effects to a few nanometers scale (Jeong *et al.*, 2005; Xiao *et al.*, 2017; Checchia *et al.*, 2016), symmetry breaking effects play a key-role on macroscopic physical properties of different classes of materials. As for the present investigation, a short-range atomic rearrangement maintains, on average, a crystallographic motif suitable for ionic conduction (channels and cages wide enough to allow the passage of ions), allowing at the same time a structural flexibility for the tetrahedra to rotate facilitating ion migration according to the cooperative mechanism proposed by Kendrick *et al.* (Kendrick *et al.*, 2007). Even though neutron diffraction would be the best technique to validate the structural details related to O ions, the present study indicates that oxygen vacancies occupy sites with different energy values, depending on their position in respect to substitutional Ba-ions. As recently pointed out by Koettgen and coworkers (Koettgen *et al.*, 2018) for a different class of oxygen ionic conductors, this should be taken into account for an accurate modelling of the oxygen migration mechanism.

*Conclusions*

DFT and PDF were combined to model the local scale structure of $La_{1-x}Ba_{1+x}GaO_{4-x/2}$. Concerning $LaBaGaO_4$, the DFT model is consistent with the reported structure. When substituting Ba for La, the PDF signals become broader indicating a larger distribution of interatomic distances, *i.e.* some structural disorder. The local structure was then investigated building four different defect configurations using DFT calculations at x=0.25. The main difference between each of them lies in the relative positions of substitutional Ba-ions with respect to the oxygen vacancy. The calculated atomic structures were used as starting point for the modelling of PDF curves on $La_{1-x}Ba_{1+x}GaO_{4-x/2}$ with x = 0.20 and 0.30. All the DFT models show the formation of $Ga_2O_7$ dimers consistently with the current literature (Kendrick *et al.*, 2007, Kitamura *et al.*, 2013, Kendrick *et al.*, 2010, Jalarvo *et al.*, 2013a). The short range PDF of doped samples (x=0.2 and x=0.3) are almost superimposed. This indicates that their local scale is very similar. Indeed, the Ga-O distance in $Ga_2O_7$ is close to the one in $GaO_4$ units, as Ga retains its tetrahedral environment.

The model giving the best fit of PDF data has substitutional Ba ions as first and second cation neighbor of the vacancy (Fig. 4). This shows that the $La_{Ba}$' defect pins the vacancy to the nearest neighbor cation site, thus affecting, in

principle, the activation energy for ionic migration. Other configurations lead to PDF patterns different than the experimental one (Fig. 6 (*a*)). Larger interatomic distances show broader PDF peaks, with the broadening increasing with doping. This indicates that the dumbbells do not order on a larger scale.

Overall, we show in this work that DFT simulations can be successfully used in synergy with XRPD-PDF to determine structural features in disordered systems. In this particular case, DFT results were utilized for the PDF fits to identify the mutual interaction of the $Ga_2O_7$ units with the $Ba_{La}$' defects. This shows that such approach may be used routinely to investigate disordered ionic conductors to get insight about how the local structure is influencing the conduction mechanism.

### *References*

Blöchl, P. E. (1994). *Phys. Rev. B: Condens. Matter Mater. Phys.* **50**, 17953−17979.

Checchia, S., Allieta, M., Coduri, M., Brunelli, M. & Scavini., M. (2016). *Phys. Rev. B* **94**, 104201.

Cheng, Y., Balachandran, J., Bi, Z., Bridges, C.A., Parans Paranthaman, M., Daemen, L. L., Ganesh, P. & Jalarvo N. (2017). *J. Mater. Chem.* A **5**, 15507−15511.

Chung, J.-H., Proffen, T., Shamoto, S.-I., Ghorayeb, A. M., Croguennec, L., Tian, W., Sales, B. C., Jin, R., Mandrus, D. & Egami, T. (2005). *Phys. Rev. B* **71**, 064410.

Coduri, M., Scavini, M., Allieta, M., Brunelli, M. & Ferrero, C. (2013), *Chem. Mater.* **25**, 4278-4289.

Coduri, M., Masala, M., Allieta, M., Peral, I., Brunelli, M., Biffi, C. A. & Scavini, M. (2018a). *Inorganic chemistry* **57**(2), 879-891.

Coduri, M., Checchia, S., M. Longhi, M., Ceresoli, D. & Scavini M. (2018b). *Frontiers in Chemistry* **6**, 526

Dagotto, M. (2005). Science **309**, 257-262.

Egami, T., & Billinge, S.J.L. (2003). Edited by R.W. Cahn. Underneath Bragg peaks. Pergamon Materials Series.

Farrow, C. L., Juhás, P., Liu, J. W., Bryndin, D., Božin, E. S., Bloch, J., Proffen, T. & Billinge, S. J. L. (2007). *J. Phys.-Condens. Matt.* **19**, 335219.

Farrow, C. L., Shaw, M., Kim, H., Juhas, P. & Billinge S. J. L. (2011). *Physical Review B* **84**, 134105.

Giannici, F., Messana, D., Longo, A. & Martorana A. (2011). *J. Phys. Chem. C* **115**, 298−304.

Giannici, F., Messana, D., Longo, A., Sciortino, L. & A. Martorana (2009). *J. Phys.: Conf. Ser.* **190**, 012077.

Hamao, N., Kitamura, N, Ishida, N., Kamiyama, T., Torii, S., Yonemura, M. & Idemoto, Y. (2014). *Electrochemistry* **82** (7), 550−556.

Hammersley, A. P., Svensson, S. O., Hanfland, M., Fitch, A. N. & Häusermann, D. (1996). *High Pressure Research* **14**, 235-248.

Jalarvo, N., Gourdon, O., Bi, Z., Gout, D., Ohl, M., & Parans Paranthaman M. (2013a). *Chem. Mater*. **25**(14), 2741–2748.

Jalarvo, N., Stingaciu, L., Gout, D., Bi, Z., Paranthaman M. P. & Ohl, M. (2013b). *Solid State Ionics* **252**, 12–18.

Jeong, I.-K., Darling, T. W., Lee, J. K., Proffen, Th., Heffner, R. H., Park, J. S. & Hong, K. S. (2005). *Phys. Rev. Lett*. **94**, 147602.

Kendrick, E., Kendrick, J., Knight, K. S., Islam, M. S. & Slater P. R. (2007). *Nature Materials* **6**, 871–875.

Kendrick, E., Knight, K. S., Islam, M. S. & Slater; P. R. (2010). *J. Mater. Chem.* **20**, 10412–10416.

Kitamura, N., Hamao, N., Vogel, S. C., Idemoto, Y. (2013) *Electrochemistry* **81**(6), 448453

Koettgen, J., Grieshammer, S., Hein, P., Grope, B. O. H., Nakayama, M. & Martin M. (2018). *Phys. Chem. Chem. Phys.* **20**, 14291-14321.

Kresse, G. & Furthmüller, J. (1996). *Comput. Mater. Sci.* **6**, 15.

Kresse, G. & Hafner, J. (1993). *Phys. Rev. B: Condens. Matter Mater. Phys.* **47**, 558−561.

Li, S., Schönberger, F. & Slater, P. (2003). *Chem. Commun.* 2694–2695.

Malavasi, L., Fischer, C. A. J. & Islam, M. S. (2010). *Chem. Soc. Rev.* **39**, 4370-4387.

Mancini, A., Tealdi, C. & Malavasi, L. (2012). *International Journal of Hydrogen Energy* **37** 8073-8080.

Page, K., Stoltzfus, M. W., Kim, Y.-I., Proffen, T., Woodward, P. M., Cheetham, A. K. & Seshadri. R. (2007). *Chem. Mater*. **19**, 4037-4042.

Perdew, J. P., Burke, K. & Ernzerhof, M. (1996). *Phys. Rev. Lett.* **77**, 3865−3868.

Pramana, S.S., Baikie, T., An, T., Tucker, M.G., Schreyer, M.K., Wei, F., Bayliss, R.D., Kloc, C. L., White, T.J., Horsfiled, A.P. & Skinner, S.J. (2016) *J. Am. Chem. Soc.* **138**(4), 1273-1279.

Qiu, X., Thompson, J. W. & Billinge S. L. J. (2004a). *J. Appl. Crystallogr.* **37**, 678.

Qiu, X., Bozin, E. S., Juhas, P., Proffen, T. & Billinge, S. J. L. (2004b). *J. Appl. Crystallogr.* **37**, 110-116.

Rüter, I. & Muller-Buschbaum H. K. (1990). *Z. anorg. allg. Chem.* **584**, 119-124.

Scavini, M., Coduri, M., Allieta, M., Brunelli, M. & Ferrero, C. (2012). *Chem. Mater*. **24**, 1338-1345.

White, C. E., Provis, J.L., Proffen, T., Riley, D. P. & van Deventer J. S. J. (2010). *Phys. Chem. Chem. Phys*. **12**, 3239–3245

Xiao, X., Widenmeyer, M., Zou, T., Xie, W., Yoon, S., Scavini, M., Checchia, S., Kilper, K., Kovalevsky, A. & Weidenkaff, A. (2017). *Phys. Chem. Chem. Phys.* **19** 13469-14680.

Yang, X., Fernàndez-Carriòn, A.J., Wang, J., Porcher, F., Fayon, F., Allix, M. & Kuang, X. (2018). *Nature Communications* **9**, 4484.